ELSEVIER

Contents lists available at ScienceDirect

### European Journal of Mechanics / B Fluids

journal homepage: www.elsevier.com/locate/ejmflu



## Compressible effects in the propagation of nonlinear shallow water waves: Models and simulations

E. Zuccoli<sup>®</sup>\*, U. Kadri

School of Mathematics, Cardiff University, Senghennydd Rd, Cardiff, CF24 4AG, United Kingdom

#### ARTICLE INFO

# Keywords: Compressible shallow-water equations Weakly nonlinear water waves Weakly dispersive water waves

#### ABSTRACT

We investigate the effects of compressibility in the propagation of shallow-water waves and extend the classical shallow-water equations to a compressible regime. Both non-dispersive and weakly-dispersive nonlinear waves are then analysed with the help of the multiple scales method, ultimately leading to the studying of a Burgers and a Korteweg-deVries equation, respectively. A parametric study is conducted in order to investigate the interplay of both nonlinearity and compressibility and assess how compressibility may alter the nonlinear properties of the waves. In particular, parameters varied are the compressibility coefficient  $\mu$ , the amplitude of the waves  $\epsilon$  and the width of the initial wave profile  $\sigma$ . In a non-dispersive regime, shock and rarefaction waves form and interact one another leading to a progressive reduction of the wave amplitude in time. The compressibility of the fluid  $\mu$  speeds up the shock formation, with beneficial effects in terms of wave amplitude reduction. In a weakly dispersive regime, on the other hand, higher compressibility values may amplify the initial perturbation, leading to the formation of a discrete number of solitons having amplitudes much greater than the amplitude at the initial stage. The analysis presented in this work aims at improving our predictions on the dynamics of nonlinear compressible shallow-water waves both in terms of wave amplitude variation and propagation time. Among various applications, our enhanced models can notably improve the estimation of tsunami arrival times and contribute to more accurate weather forecasts. Furthermore, the work presented here lays the foundation for future experimental studies and assessments in this field.

#### 1. Introduction

Geophysical flows are large scale motions developing in oceans and atmosphere. They typically occur over very large horizontal spatial scales compared to their depths, so that vertical accelerations can usually be neglected.

Mathematically, atmospheric and oceanic flows are modelled using the shallow-water approximation [1], which allows to reduce the complete three-dimensional Navier–Stokes equations to a two-dimensional system of equations defined in terms of surface variables only, bringing a huge advantage in terms of computational costs. The shallow-water equations also support the propagation of nonlinear waves, and possess nice mathematical features—e.g. strictly hyperbolicity—useful to accurately describe shock and rarefaction waves [2], tidal waves [3], and provide nonlinear analogues with systems in other fields [4].

However, the reduction in the mathematical complexity of the problem is replaced by a lack in the accuracy of the description of wave motions within certain regimes; for example, dispersive effects come into play very soon and need to be included in the models. The first attempt to do so was carried out by Boussinesq [5], who derived

a dispersive wave equation taking into account the effects of depth. Boussinesq equations and subsequent models are all derived by depth-averaging the incompressible Euler equations under the assumption of weak nonlinearity. Improved models giving rise to either classical Burgers or Korteweg–deVries equations have been proposed by Su and Gardner [6], Green and Naghdi [7] in the case of fully nonlinear waves, and by Bonneton et al. [8], Brocchini [9], Kirby [10] when dispersion is no more weak. Other physical mechanisms included in shallow-water models comprise Earth rotation [11–13] and viscous dissipation [14,15].

All models previously mentioned have been derived under the assumption of considering the flow as incompressible. However, in recent years, compressible effects have been shown to influence the propagation of ocean surface gravity modes through their nonlinear resonant interaction with acoustic compressible modes propagating all over the fluid layer. This coupling has been shown to be responsible for the continuous exchange of energy among a small number of linear modes [16–20], ultimately leading to a modest reduction in

E-mail address: ZuccoliE@cardiff.ac.uk (E. Zuccoli).

<sup>\*</sup> Corresponding author.

the amplitude of the gravity wave when the latter interacts with two acoustic waves [21].

The main motivation behind the present work is to investigate the effects of compressibility in the dynamics of weakly nonlinear shallowwater waves. Following the statement in McWilliams' book [11, pp. 47]: "Earth's atmosphere has vertical profiles much closer to isothermal than isentropic...", as well as the works of Kadri and Akylas [17], Longuet-Higgins [22], we assume all fluids considered in this work to be barotropic and isothermal, such that the pressure varies linearly with the density only, namely  $P = P(\rho) = P_a + c^2(\rho - \rho_a)$ , where c is the constant speed of sound,  $P_a$  the atmospheric pressure and  $\rho_a$  the constant value of the density on the fluid's free surface. We are going to generalize the classical shallow-water equations to the compressible case and, starting from the resulting system, derive two reduced models that could be used in place of the full general equations. These two models are a compressible Burgers equation (CB), for the modelling of non-dispersive, weakly nonlinear compressible waves and a compressible Korteweg-deVries equation (CKdV), for the modelling of weakly dispersive, weakly nonlinear compressible waves. The focus of the paper is to evaluate the effects of both nonlinearity and compressibility, thus a parametric study will be carried out to describe different solutions and regimes of propagation of compressible shallowwater waves. As it will be shown in the next sections, compressibility can ultimately lead to quite substantial differences in the quantitative prediction of shallow-water waves with respect to their incompressible counterparts, hence improving our capacity of better capturing the dynamics of these type of phenomena. This could be also beneficial from a more experimental perspective, in view of designing more accurate and reliable risk assessment devices concerning the propagation of either tsunamis or strong winds in the atmosphere.

The paper is organized as follows: in Section 2 we derive the compressible shallow-water equations both in a non-dispersive and in a weakly dispersive regime following the scaling by Johnson [23]. To this end, we are going to extensively use the method of multiple scales [24–26]. In Section 3 we conduct our parametric study and show results for the derived models in both non-dispersive and weakly dispersive regimes, and compare solutions with the corresponding incompressible ones. Importance of both nonlinearity and compressibility will also be shown, together with a convergence study on the reduced models. Finally, in Section 4 we draw conclusions and possible future research perspectives.

#### 2. Problem definition and scaling

Let us consider a compressible, inviscid, barotropic fluid which extends vertically from a rigid wall located at z=-h to an upper free surface described by a function  $\eta(x_H,t)$ . Here  $x_H$  denotes horizontal spatial coordinates, so the position of each fluid particle can be defined as  $x=x_H+z\hat{z}$ . Similarly, the velocity, pressure and density fields are defined as  $u=u_H(x,t)+u_z(x,t)\hat{z}$ , P=P(x,t),  $\rho=\rho(x,t)$ . The governing equations are the compressible Euler equations expressing conservation of horizontal and axial momentum, and conservation of mass, respectively:

$$\rho \partial_t \mathbf{u}_H + \rho (\mathbf{u}_H \cdot \nabla_H) \mathbf{u}_H + \rho \mathbf{u}_z \partial_z \mathbf{u}_H + \nabla_H P = 0, \tag{1a}$$

$$\rho \partial_t u_z + \rho (\mathbf{u}_H \cdot \nabla_H u_z) + \rho u_z \partial_z u_z + \partial_z P + g \rho = 0, \tag{1b}$$

$$\partial_t \rho + \rho (\nabla \cdot \mathbf{u}) + \mathbf{u} \cdot \nabla \rho = 0, \tag{1c}$$

where  $\nabla_H$  expresses the gradient along the horizontal coordinates, and g is the acceleration due to gravity. The fluid must satisfy a nopenetration boundary condition  $u_z=0$  at z=-h and two free surface boundary conditions along the free surface itself

$$P = P_a$$
, and  $u_z = \partial_t \eta + u_H \cdot \nabla_H \eta$ , on  $z = \eta$ , (2)

with  $P_a$  being the atmospheric constant pressure above the fluid layer. Finally, the thermodynamic relationship  $P(\rho)=P_a+c^2(\rho-\rho_a)$  is needed to close the system.

We proceed to the non-dimensionalization of the differential problem above by defining three different length scales:  $\lambda$  characterizing the horizontal wavelength of the waves, h the depth of the fluid and a a typical amplitude of the wave. Moreover, we consider waves travelling with characteristic velocity  $\sqrt{gh}$ . Variables are then scaled as follows

$$\begin{aligned} & \boldsymbol{x}_{H} = \lambda \tilde{\boldsymbol{x}}_{H}; \quad \boldsymbol{z} = h\tilde{\boldsymbol{z}}; \quad \boldsymbol{t} = \frac{\lambda}{\sqrt{gh}} \tilde{\boldsymbol{t}}; \\ & \boldsymbol{\eta} = a\tilde{\boldsymbol{\eta}}; \quad \boldsymbol{\rho} = \boldsymbol{\rho}_{a}\tilde{\boldsymbol{\rho}}; \quad \boldsymbol{P} = \boldsymbol{\rho}_{a}ag\tilde{\boldsymbol{P}}; \quad \boldsymbol{u}_{H} = \frac{a\sqrt{gh}}{h} \tilde{\boldsymbol{u}}_{H}; \quad \boldsymbol{u}_{z} = \frac{a\sqrt{gh}}{\lambda} \tilde{\boldsymbol{u}}_{z}, \end{aligned} \tag{3}$$

where tilde symbol is used for non-dimensional variables. Upon substitution into the governing equations and boundary conditions—after dropping the tilde symbol for readability—our general differential problem in dimensionless form reads

$$\rho \partial_t u_H + \epsilon \left[ \rho(u_H \cdot \nabla_H) u_H + \rho u_z \partial_z u_H \right] + \nabla_H P = 0, \tag{4a}$$

$$\delta^{2} \left[ \rho \partial_{t} u_{z} + \epsilon \rho \mathbf{u} \cdot \nabla u_{z} \right] + \partial_{z} P + \frac{1}{\epsilon} \rho = 0, \tag{4b}$$

$$\partial_t \rho + \epsilon \nabla \cdot \left( \rho \mathbf{u} \right) = 0, \tag{4c}$$

$$P(\rho) = P_a + \frac{1}{\epsilon u} (\rho - 1), \tag{4d}$$

$$P = P_a$$
, and  $u_z = \partial_t \eta + \epsilon u_H \cdot \nabla_H \eta$ , on  $z = \epsilon \eta$ , (4e)

$$u_z = 0, \quad \text{on} \quad z = -1, \tag{4f}$$

where we have defined the three parameters

$$\delta = \frac{h}{\lambda}, \quad \epsilon = \frac{a}{h}, \quad \mu = \frac{gh}{c^2}.$$
 (5)

In particular,  $\delta$  measures the importance of dispersive effects associated to the regime of propagation of the waves (i.e. shallow-water when  $\delta \ll 1$ , deep-water when  $\delta \gg 1$ ). Parameter  $\epsilon$  is a measure of the nonlinearity of the system; this is meaningful in shallow water, in contrast to deep water where the nonlinearity is usually measured by the wave steepness  $a/\lambda$ . Parameter  $\mu$  measures the importance of compressibility effects in the fluid and is a crucial parameter in the models we are going to derive later on. It will be kept, in fact, as an arbitrary parameter so that its importance can be directly measured in the new models derived. This is justified from a mathematical point of view provided the new models are consistent with those already established in the literature; in our case, the incompressible models. An analogous approach can be found in Johnson [23] on the treatment of capillarity effects. Note that the dimensionless speed of sound in (4d) goes to infinity as  $\mu \to 0$ , in accordance with the incompressible limit.

#### 2.1. Nonlinear, non-dispersive compressible shallow water waves $\delta^2 \ll \epsilon$

When dispersive effects are negligible compared to nonlinear effects, the so-called shallow-water approximation holds and the convective term in the axial momentum equation becomes negligible. It immediately follows from (4b)

$$\partial_z P = -\frac{1}{\epsilon} \rho \quad \Rightarrow \quad \partial_z P = -\mu P - \frac{1 - \mu \epsilon P_a}{\epsilon},$$
 (6)

which after imposing the dynamic boundary condition in (4e) yields

$$P(\mathbf{x}_H, z, t) = P_a + \frac{1}{\mu \epsilon} \left[ e^{\mu(\epsilon \eta - z)} - 1 \right], \quad \text{and} \quad \rho(\mathbf{x}_H, z, t) = e^{\mu(\epsilon \eta - z)}. \tag{7}$$

Note that for  $\mu \to 0$  ( $c \to \infty$ ), Eq. (7) returns the more familiar linear hydrostatic pressure contribution valid in the incompressible regime. Now, let us define for notation brevity  $E=e^{\mu(\epsilon\eta-z)}$ . Inserting (7) into the horizontal momentum equation, we obtain

$$\mu \epsilon \left[ \partial_t \mathbf{u}_H + \epsilon (\mathbf{u}_H \cdot \nabla) \mathbf{u}_H + \epsilon \mathbf{u}_z \partial_z \mathbf{u}_H \right] E + \left[ \mu \epsilon \nabla_H \eta \right] E = 0. \tag{8}$$

As  $\eta$  does not depend on z,  $u_H$  does not too, so after simplifying the exponential term we get the final shallow-water momentum equation

$$\partial_t \mathbf{u}_H + \epsilon (\mathbf{u}_H \cdot \nabla_H) \mathbf{u}_H + \nabla_H \eta = 0, \tag{9}$$

which is identical to the momentum equation in the incompressible case.

Regarding the mass conservation equation, after computing the derivatives and cancelling the common exponential factor, we are left with

$$\partial_z u_z - \mu u_z = -\mu \partial_t \eta - \mu \epsilon \mathbf{u}_H \cdot \nabla_H \eta - \nabla_H \cdot \mathbf{u}_H \equiv -f(\mathbf{x}_H, t), \tag{10}$$

whose solution after imposing the no-penetration boundary condition at z=-1 reads

$$u_z(\mathbf{x},t) = \frac{f(\mathbf{x}_H,t)}{\mu} \left[ 1 - e^{\mu(z+1)} \right], \quad \text{with} \quad f(\mathbf{x}_H,t) = \mu \partial_t \eta + \mu \epsilon \mathbf{u}_H \cdot \nabla_H \eta + \nabla_H \cdot \mathbf{u}_H.$$
(11)

Imposition of the additional kinematic boundary condition at the free surface  $z=\epsilon\eta$  produces—after exploiting the definition of  $f(x_H,t)$ 

$$\partial_t \eta + \epsilon (\boldsymbol{u}_H \cdot \nabla_H \eta) + \frac{1}{\mu} (\nabla_H \cdot \boldsymbol{u}_H) \left[ 1 - e^{-\mu(\epsilon \eta + 1)} \right] = 0.$$
 (12)

Eq. (12) is the new evolution equation for the free surface elevation. It takes into account the effects of compressibility through the last term in square brackets. Combining (9) and (12), the final compressible shallow water equations (CSWE) read

$$\partial_t \mathbf{u}_H + \epsilon (\mathbf{u}_H \cdot \nabla_H) \mathbf{u}_H + \nabla_H \eta = 0, \tag{13a}$$

$$\partial_t \eta + \epsilon (\boldsymbol{u}_H \cdot \nabla_H \eta) + \frac{1}{u} (\nabla_H \cdot \boldsymbol{u}_H) \left[ 1 - e^{-\mu(\epsilon \eta + 1)} \right] = 0.$$
 (13b)

Note that system (13) is consistent with the corresponding incompressible limit  $\mu \to 0$ .

#### 2.1.1. Reduced order wave propagation model 1

In this section we assume  $\epsilon \ll 1$  and obtain a reduced model by means of a weakly nonlinear analysis. The parameter  $\mu$  is arbitrarily fixed, so that an asymptotic expansion can be made around  $\epsilon = 0$  only. Here we work with Eqs. (13a)–(13b) in one spatial dimension x.

We start by Taylor-expanding the last term within square brackets in (13b), obtaining:

$$1 - e^{-\mu(\epsilon \eta + 1)} = 1 - e^{-\mu} \left[ 1 - \mu \epsilon \eta + \frac{\mu^2 \epsilon^2}{2} \eta^2 + \mathcal{O}(\epsilon^3) \right]. \tag{14}$$

Combining this with the momentum equation we have

$$\partial_t u + \epsilon u \partial_x u + \partial_x \eta = 0, \tag{15a}$$

$$\partial_t \eta + \epsilon u \partial_x \eta + \partial_x u \left( c_\mu^2 + e^{-\mu} \epsilon \eta - \mu e^{-\mu} \frac{\epsilon^2}{2} \eta^2 \right) = 0, \tag{15b}$$

where  $c_{\mu}=\sqrt{(1-e^{-\mu})/\mu}$  is the constant phase speed in compressible shallow-water linear waves [27]. In order to make progress and study the weakly nonlinear dynamics of the system, we apply the method of multiple scales and introduce a slow time scale  $\tau=\epsilon t$ . For simplicity, we just look for travelling waves moving to the right, i.e. we define the characteristic coordinate  $\xi=x-c_{\mu}t$  and assume

$$u(x,t,\tau) = u(\xi,\tau), \quad \text{and} \quad \eta(x,t,\tau) = \eta(\xi,\tau).$$
 (16)

System (15) becomes

$$-c_{\mu}\partial_{\xi}u + \partial_{\xi}\eta = -\epsilon \Big(\partial_{\tau}u + u\partial_{\xi}u\Big), \tag{17a}$$

$$-c_{\mu}\partial_{\xi}\eta + c_{\mu}^{2}\partial_{\xi}u = -\epsilon \left(\partial_{\tau}\eta + u\partial_{\xi}\eta + e^{-\mu}\eta\partial_{\xi}u\right) + \frac{\epsilon^{2}}{2}\mu e^{-\mu}\eta^{2}\partial_{\xi}u. \tag{17b}$$

At this point we expand the unknowns in power series of  $\epsilon$ 

$$u(\xi,\tau) = u_0(\xi,\tau) + \epsilon u_1(\xi,\tau) + \mathcal{O}(\epsilon^2), \quad \text{and} \quad \eta(\xi,\tau) = \eta_0(\xi,\tau) + \epsilon \eta_1(\xi,\tau) + \mathcal{O}(\epsilon^2),$$

and plug them into (17). At leading order, the solution gives  $\eta_0 = A(\xi, \tau)$  together with  $u_0 = A(\xi, \tau)/c_\mu$ , where A is still a function to be

determined by solving the system at the next order. At order  $\epsilon$ , the system to be solved reads

$$-c_{\mu}\partial_{\varepsilon}u_{1} + \partial_{\varepsilon}\eta_{1} = -\partial_{\tau}u_{0} - u_{0}\partial_{\varepsilon}u_{0}, \tag{19a}$$

$$-c_{\mu}\partial_{\varepsilon}\eta_{1} + c_{\mu}^{2}\partial_{\varepsilon}u_{1} = -\partial_{\tau}\eta_{0} - u_{0}\partial_{\varepsilon}\eta_{0} - e^{-\mu}\eta_{0}\partial_{\varepsilon}u_{0}, \tag{19b}$$

which after some algebra returns the amplitude equation

$$\partial_{\tau}A + \alpha(\mu)A\partial_{\xi}A = 0$$
, with  $\alpha(\mu) = \frac{e^{-\mu}}{2c_{\mu}}\left(1 + 2e^{\mu}\right)$ . (20)

Eq. (20) is a compressible Burgers equation for the fluid elevation  $A(\xi,\tau)$  and can be solved either analytically and numerically using standard methods for nonlinear hyperbolic equations. The effects of compressibility have implications on the strength of the nonlinear term, leading to changes in both the propagation speed and shape of the wave.

#### 2.2. Hyperbolic properties of the compressible shallow-water equations

We consider the system of Eqs. (13) in one spatial dimension. Following [2], it can be written in conservative form as

$$\partial_t H + \partial_x (vH) = 0, (21a)$$

$$\partial_t(vH) + \partial_x \left[ v^2 H + \frac{1}{\mu} \left( H - \frac{1}{\mu} \log(1 + \mu H) \right) \right], \tag{21b}$$

where  $H = (e^{\mu(\epsilon\eta+1)} - 1)/\mu$ ,  $v = \epsilon u$ . We define the momentum per unit volume m = vH and introduce the state vector  $\boldsymbol{w} = (H, m)^T$ , so that Eqs. (21) can be compactly written as

$$\partial_t \mathbf{w} + \partial_{\mathbf{x}} \mathbf{f}(\mathbf{w}) = 0, \tag{22}$$

where the flux function takes the form

$$f(w) = \left(m, \frac{m^2}{H} + \frac{1}{u} \left(H - \frac{g}{u} \log(1 + \mu H)\right)\right)^T.$$
 (23)

This formulation ensures the entropy condition is satisfied in case of shocks formation [2,28,29]. This is in accordance with the equivalent statement that an entropy-satisfying solution can be seen as the limit of the corresponding vanishing viscosity solution [30]. In Appendix C we derive an energy equation for the Burgers model showing energy loss at shock waves. Even though the energy equation can be generalized in case of nonlinear hyperbolic systems following the derivation in [30, pp. 7–10], this task falls outside the objectives of the present study, so we do not provide such a generalization here. However, due to the high accuracy between the full numerical solutions and the Burgers solutions (this will be shown in the next sections), the derivation of the energy equation for the Burgers model gives an exhaustive insight and comprehension of the mechanisms involved in energy dissipation occurring at shocks formation.

In order to study the hyperbolic properties of Eqs. (21), it is convenient re-write them in quasilinear form  $\partial_t w + A(w)\partial_x w = 0$ , where the Jacobian matrix A(w) is defined as

$$\mathbf{A}(\mathbf{w}) = \frac{\partial \mathbf{f}(\mathbf{w})}{\partial \mathbf{w}} = \begin{pmatrix} 0 & 1\\ -\frac{m^2}{H^2} + \frac{H}{1+uH} & 2\frac{m}{H}. \end{pmatrix}$$
(24)

The characteristic velocities of the system are given by the eigenvalues of A(w), namely

$$\lambda_1(\mathbf{w}) = \frac{m}{H} - \left(\frac{H}{1 + \mu H}\right)^{1/2}, \text{ and } \lambda_2(\mathbf{w}) = \frac{m}{H} + \left(\frac{H}{1 + \mu H}\right)^{1/2},$$
 (25)

whose corresponding right eigenvectors are

$$\mathbf{r}_1(\mathbf{w}) = \begin{pmatrix} H \\ m - \left(\frac{H^3}{1+\mu H}\right)^{1/2} \end{pmatrix}, \text{ and } \mathbf{r}_2(\mathbf{w}) = \begin{pmatrix} H \\ m + \left(\frac{H^3}{1+\mu H}\right)^{1/2} \end{pmatrix}.$$
 (26)

Note that the eigensolutions for a nonlinear hyperbolic system depend on the state variables H and m. The character of the nonlinear waves

supported by the CSWE (21) is dictated by the so-called "nonlinearity factor"

$$\omega_i(\boldsymbol{w}) = \frac{\boldsymbol{r}_i(\boldsymbol{w}) \cdot \nabla_{\boldsymbol{w}} \lambda_i(\boldsymbol{w})}{H^{1/2}}, \quad i = 1, 2,$$
(27)

with  $\nabla_w = (\partial_H, \partial_m)^T$  being the gradient operator along the state variables (H, m). For the two eigenvalues and eigenfunctions of the nonlinear system, we have

$$\omega_{1,2}(\mathbf{w}) = \mp \left(\frac{1}{1+\mu H}\right)^{1/2} \left[1 + \frac{1}{2(1+\mu H)}\right] \neq 0 \quad \forall (H, m),$$
 (28)

since  $1 + \mu H = e^{\mu(\epsilon\eta+1)} > 0$ . Therefore both eigenvalues are genuinely nonlinear and the system can support the propagation of either shock and rarefaction waves, but not of contact discontinuities (unlike for the classical gasdynamics equations [31]). These features can be useful to study a Riemann problem for Eqs. (21) whose solution would consist in a combination of either two shocks, or one shock together with one rarefaction, or two rarefactions. Despite the relevant applications (e.g. dam-break-like problems, bores propagation), the study of Riemann problems for Eqs. (21) is out of scope of the present work. Nevertheless, interested readers can find more details on a similar model (isothermal ideal gasdynamics problem) in Fossati and Ouartapelle [32]

## 2.3. Nonlinear, weakly dispersive compressible shallow water waves $\delta^2 = \mathcal{O}(\epsilon)$

In the previous section we derived models valid under the shallow water approximation, i.e. when  $\delta^2 \ll \epsilon$ . Now, we relax that assumption by allowing  $\delta^2 = \mathcal{O}(\epsilon)$  in Eq. (4b), as well as the flow to be two-dimensional  $\mathbf{u} = u(x,z,t)\hat{\mathbf{x}} + w(x,z,t)\hat{\mathbf{z}}, \ P = P(x,z,t), \ \rho = \rho(x,z,t)$  and  $\eta = \eta(x,t)$ . System (4) can then be re-written more compactly and conveniently as

$$\partial_t u + \epsilon \left( u \partial_x u + w \partial_z u \right) + \partial_x q = 0, \tag{29a}$$

$$\delta^{2} \left[ \partial_{t} w + \epsilon \left( u \partial_{x} w + w \partial_{z} w \right) \right] + \partial_{z} q = 0, \tag{29b}$$

$$\mu \left[ \partial_t q + \epsilon \left( u \partial_x q + w \partial_z q \right) - w \right] + \partial_x u + \partial_z w = 0, \tag{29c}$$

$$q = \eta$$
, and  $w = \partial_t \eta + \epsilon u \partial_x \eta$ , on  $z = \epsilon \eta$ , (29d)

$$w = 0$$
, on  $z = -1$ . (29e)

where the "new pressure"  $\boldsymbol{q}$  is related to  $\boldsymbol{\rho}$  via the transformation

$$\log(\rho) = -\mu z + \log(\mu \epsilon) + \mu \epsilon q. \tag{30}$$

#### 2.3.1. Reduced order wave propagation model 2

Following [23, ch. 3], we take  $\delta^2 = \epsilon$  and introduce the slow time scale  $\tau = \epsilon t$ . After expanding the boundary conditions (29d) in Taylor series around z=0 and retaining terms of at most order  $\epsilon$ , we obtain the problem

$$\partial_t u + \partial_x q + \epsilon \left( \partial_\tau u + u \partial_x u + w \partial_z u \right) = 0, \tag{31a}$$

$$\partial_z q + \epsilon \partial_t w = 0, (31b)$$

$$\partial_z w - \mu w + \mu \partial_t q + \partial_x u + \epsilon \mu \left( \partial_\tau q + u \partial_x q + w \partial_z q \right) = 0, \tag{31c}$$

$$q = \eta - \epsilon \eta \partial_z q$$
, and  $w = \partial_t \eta + \epsilon \left( \partial_\tau \eta + u \partial_x \eta - \eta \partial_z w \right)$ , on  $z = 0$ , (31d)

$$w = 0$$
, on  $z = -1$ . (31e)

We now expand our unknowns in powers of  $\epsilon$  as

$$(u, w, q, \eta) = (u_0, w_0, q_0, \eta_0) + \epsilon(u_1, w_1, q_1, \eta_1) + \mathcal{O}(\epsilon^2), \tag{32}$$

so after collecting terms of the same order, the following two differential problems need to be solved:

$$\mathcal{O}(1): \quad \partial_t u_0 + + \partial_x q_0 = 0, \tag{33a}$$

$$\partial_z q_0 = 0, (33b)$$

$$\partial_z w_0 - \mu w_0 + \mu \partial_t q_0 + \partial_x u_0 = 0,$$
 (33c)

$$q_0 = \eta_0$$
, and  $w_0 = \partial_t \eta_0$ , on  $z = 0$ , (33d)

$$w_0 = 0$$
, on  $z = -1$ . (33e)

$$\mathcal{O}(\epsilon): \quad \partial_t u_1 + \partial_x q_1 = -\partial_x u_0 - u_0 \partial_x u_0 - w_0 \partial_x u_0, \tag{34a}$$

$$\partial_z q_1 = -\partial_t w_0, \tag{34b}$$

$$\partial_z w_1 - \mu w_1 + \mu \partial_t q_1 + \partial_x u_1 = -\mu \Big( \partial_\tau q_0 + u_0 \partial_x q_0 + w_0 \partial_z q_0 \Big),$$

 $q_1 = \eta_1 - \eta_0 \partial_z q_0$ , on z = 0, (34d)

(34c)

$$w_1 = \partial_t \eta_1 + \partial_\tau \eta_0 + u_0 \partial_x \eta_0 - \eta_0 \partial_z w_0$$
, on  $z = 0$ , (34e)

$$w_1 = 0$$
, on  $z = -1$ . (34f)

We again search for travelling wave solutions in the positive x-direction, as in (16). The system at leading order readily returns

$$\eta_0(x, z, t, \tau) = A(\xi, \tau), \quad u_0(x, z, t, \tau) = \frac{1}{c_\mu} A(\xi, \tau), 
w_0(x, z, t, \tau) = \left(\frac{1}{\mu c_\mu} - c_\mu\right) \left[1 - e^{\mu(z+1)}\right] \partial_{\xi} A.$$
(35)

Regarding the problem at order  $\epsilon$ , we can immediately integrate the axial momentum equation, and after imposing the dynamic boundary condition, we get the pressure distribution

$$q_{1}(\xi,z,\tau) = \frac{1 - \mu c_{\mu}^{2}}{\mu} \left[ z - \frac{e^{\mu}}{\mu} \left( e^{\mu z} - 1 \right) \right] \partial_{\xi}^{2} A + \eta_{1}. \tag{36}$$

Now, from (34a) we can compute  $\partial_\xi u_1$  as function of  $q_1$  and insert it into (34c). Using the dynamic and kinematic boundary conditions (34d)–(34e) we end up with the following differential problem in  $w_1$  only

$$\partial_{z}w_{1} - \mu w_{1} = \left(\mu c_{\mu} - \frac{1}{c_{\mu}}\right) \left(\frac{1 - \mu c_{\mu}^{2}}{\mu}\right) \left[z - \frac{e^{\mu}}{\mu} \left(e^{\mu z} - 1\right)\right] \partial_{\xi}^{3} A$$

$$+ \left(\mu c_{\mu} - \frac{1}{c_{\mu}}\right) \partial_{\xi} \eta_{1}$$

$$- \left(\mu + \frac{1}{c_{\mu}^{2}}\right) \partial_{\tau} A - \frac{1}{c_{\mu}} \left(\mu + \frac{1}{c_{\mu}^{2}}\right) A \partial_{\xi} A, \tag{37a}$$

$$w_{1} = \partial_{\tau} A + \left[\frac{1}{c_{\mu}} + e^{\mu} \left(\frac{1}{c_{\mu}} - \mu c_{\mu}\right)\right] A \partial_{\xi} A - c_{\mu} \partial_{\xi} \eta_{1}, \text{ on } z = 0, \tag{37b}$$

$$w_1 = 0$$
, on  $z = -1$ , (37c)

whose solution returns (after some algebra) the compressible Korteweg–de Vries (CKdV) equation

$$\partial_{\tau} A + \alpha(\mu) A \partial_{\varepsilon} A = \beta(\mu) \partial_{\varepsilon}^{3} A, \tag{38}$$

with coefficients

$$\alpha(\mu) = \frac{e^{-\mu}}{2c_{-\mu}} \left( 1 + 2e^{\mu} \right),\tag{39a}$$

$$\beta(\mu) = \frac{e^{-\mu}}{2} \left( \mu c_{\mu} - \frac{1}{c_{\mu}} \right) \left( 1 - \mu c_{\mu}^{2} \right) \frac{1}{\mu^{3}} \left[ (e^{\mu} - 1)(e^{\mu} + 1) - 2\mu e^{\mu} \right].$$
 (39b)

Again, the model is consistent with its incompressible limit. In fact, when  $\mu \to 0$ , we have  $\alpha = 3/2$  and  $\beta = -1/6$  which yields the incompressible KdV equation  $\partial_{\tau} A + (3/2)A\partial_{\xi} A + (1/6)\partial_{\xi}^3 A = 0$ —see e.g. [23, p.208].

#### 3. Results

We solve both the complete differential problem (13) and the reduced models (20)-(38), and make comparison between them. As

**Table 1**Typical values of the parameters and corresponding physical quantities of interest (wave amplitude, wavelength, water depth) for laboratory, oceanic and atmospheric conditions.

	c [m/s]	h [m]	a [m]	λ [m]	$\epsilon$	δ	μ
Lab	1500	1.5	≤0.6	10	≤0.4	0.1	$6.54 \cdot 10^{-6}$
Ocean	1500	4000	≤1	$10^{5}$	$\leq 2.5 \cdot 10^{-4}$	0.04	0.01744
Atmosphere	343	20 000	≤2000	$10^{5}$	≤0.1	0.2	1.6677

previously noted,  $\mu$  is treated as an arbitrary parameter within our equations and the analysis is restricted to waves moving along the single spatial coordinate x. We envision this study to be representative of a broad class of phenomena involving the propagation of nonlinear shallow-water waves in a generic fluid. This might include the modelling and simulation of tsunamis, bores, rogue waves, atmospheric gravity waves and weather predictions, among others. To investigate the models discussed above and make comparisons between them, we consider three representative physical environments: laboratory-scale settings, the ocean, and the atmosphere. Typical values of the parameters of interest for the three specific scenarios are summarized in Table 1.

In order to validate results, both Eqs. (13) and (20) are solved twice using two different numerical methods: the method of lines (MOL) [33] and a finite difference method with Roe's numerical flux for nonlinear hyperbolic systems [2]. Solutions coming from both methods have then been compared and result in good agreement. However, the MOL is more efficient as it allows to save computational time, as well as to provide less dissipative solutions for longer times. Therefore, hereafter, we show numerical results from the MOL simulations only. Further details are contained in Appendix A. Eq. (38) is also solved using the MOL.

#### 3.1. Results for model 1: full numerical simulations

In this section we show results for the 1D compressible shallow water Eqs. (13). The initial conditions are taken in the form

$$\eta(x,0) = e^{-x^2/\sigma^2}$$
, and  $u(x,0) = 0$ , (40)

where  $\sigma$  defines the initial width of the surface perturbation normalized by the horizontal wavelength. This parameter is varied in the simulations spanning  $\sigma \in [1/2\pi, L/2\pi\lambda]$ , with L defining the size of the computational domain used in the three different environments, i.e.  $L = [63, 10^6, 10^6]$  [m] for the lab, ocean and atmosphere cases, respectively. The other parameter being varied throughout the simulations is the dimensionless amplitude of the surface waves  $\epsilon$ . In particular, for the lab environment we take  $\epsilon \in [0.001, 0.4]$ . For the ocean we take  $\epsilon \in [2.5 \cdot 10^{-4}, 0.1]$ , whereas for the atmospheric environment we take  $\epsilon = [0.001, 0.1]$ . The choice of gaussian initial conditions is probably the simplest way to analyse and control the wave dynamics, focussing on the interplay between nonlinearity and compressibility. Regarding the maximum values of  $\epsilon$  considered,  $\epsilon_{\max} =$ 0.4 for the laboratory case represents well an average maximum wave height achievable in standard laboratories. The choice of  $\epsilon_{\rm max} = 0.1$  for oceans, although being far too large in standard conditions, is mostly dictated by two reasons: first, to see under which set of parameters nonlinearity comes into play in ocean dynamics. Second, the need to test the robustness of our models, especially in capturing shocks formation. The same holds for atmospheric conditions, although in this environment  $\epsilon \simeq 0.1$  is still possible in real situations.

In order to quantify the effects of both nonlinearity and compressibility, we define the normalized  $L_2$ -error between the linear solutions  $\eta_L \equiv \eta(\epsilon=0)$  and the corresponding nonlinear ones  $\eta$  on one hand, and between  $\eta$  and the corresponding incompressible solutions  $\eta_i \equiv \eta(\mu=0)$ 

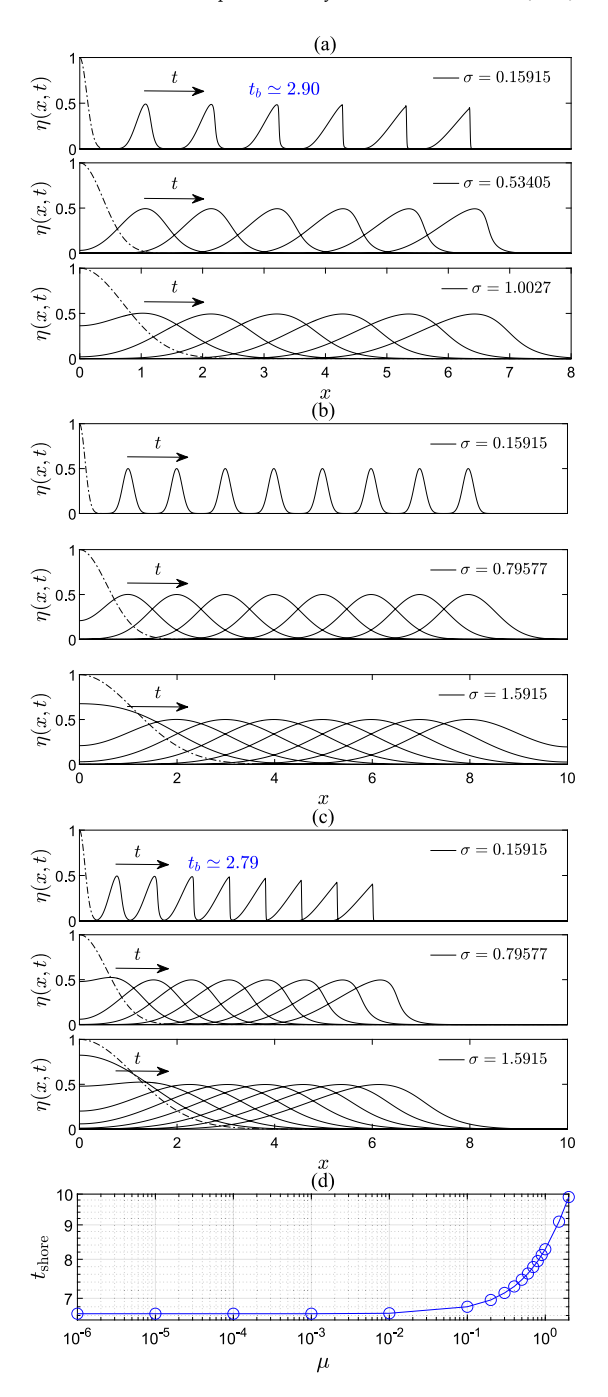


**Fig. 1.** Snapshots at different times of the full numerical solutions computed for three values of  $\sigma$ . (a): lab,  $\epsilon = 0.1$ ,  $t = 0, 1, \ldots, 6$ . (b): ocean,  $\epsilon = 2.5 \cdot 10^{-4}$ ,  $t = 0, 1, \ldots, 10$ . (c): atmosphere,  $\epsilon = 0.1$ ,  $t = 0, 1, \ldots, 10$ . The initial profiles are displayed with a dash-dotted line and the breaking time is shown in blue. (d): Arrival time of the wave at x = 7. (For interpretation of the references to colour in this figure legend, the reader is referred to the web version of this article.)

on the other, namely

$$\begin{split} D_{\epsilon}(t;\epsilon,\sigma,\mu) &= \int_{0}^{L} |\eta_{L}(x,t;\sigma,\mu) - \eta(x,t;\epsilon,\sigma,\mu)|^{2} \mathrm{d}x \Big/ \int_{0}^{L} |\eta_{L}(x,0;\sigma,\mu)|^{2} \mathrm{d}x, \\ Q_{\mu}(t;\epsilon,\sigma,\mu) &= \int_{0}^{L} |\eta_{i}(x,t;\epsilon,\sigma) - \eta(x,t;\epsilon,\sigma,\mu)|^{2} \mathrm{d}x \Big/ \int_{0}^{L} |\eta_{i}(x,0;\epsilon,\sigma)|^{2} \mathrm{d}x. \end{split}$$

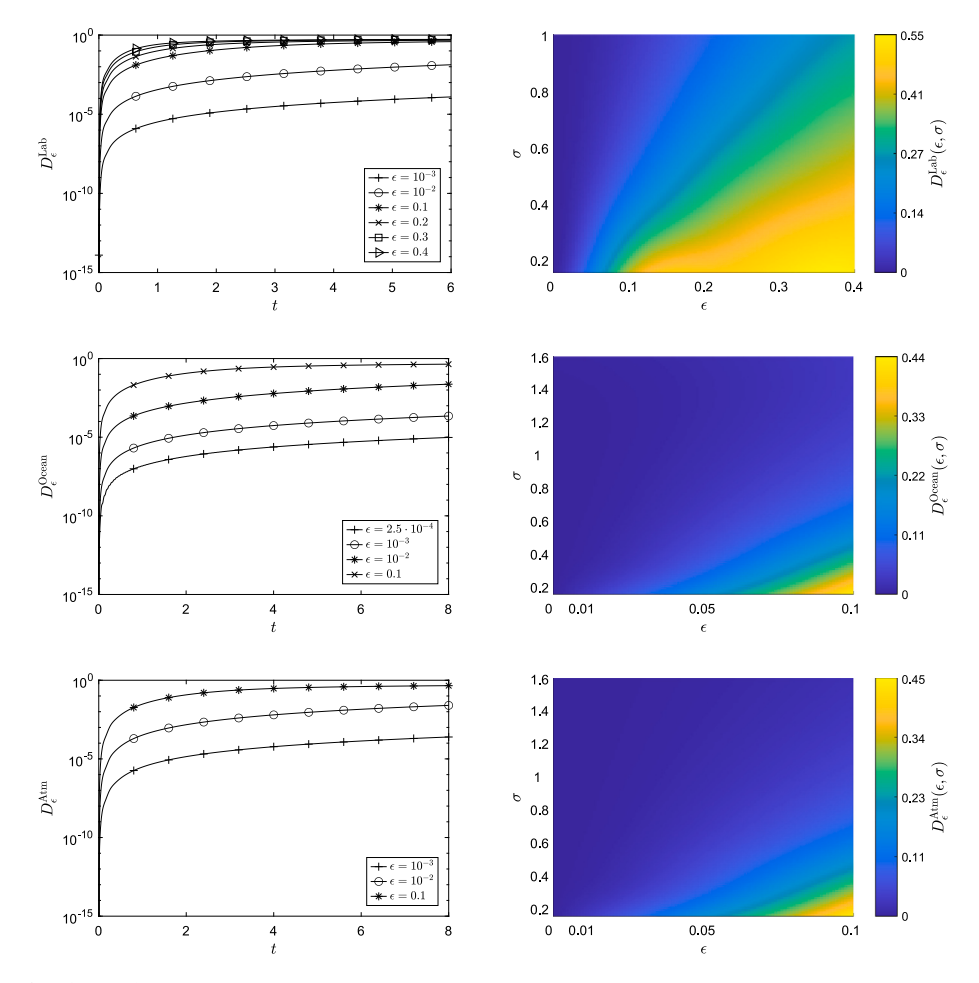


Fig. 2. Error function  $D_{\epsilon}^{\text{Lab}}$ ,  $D_{\epsilon}^{\text{Ocean}}$ ,  $D_{\epsilon}^{\text{Atm}}$  for the three scenarios. Left panels: logarithmic behaviour in time for  $\sigma = 1/2\pi$  and different  $\epsilon$ . Right panels: error behaviour at the final simulation time as function of  $\sigma$  and  $\epsilon$ .

We start by showing typical solutions for each scenario, computed for three values of  $\sigma$  and either  $\epsilon = 2.5 \cdot 10^{-4}$  (Fig. 1(b)) or  $\epsilon = 0.1$  (Fig. 1(a, c)). For panel (b) the dynamics is linear as  $\epsilon$  is extremely small and the wave simply moves to the right without changing its shape and speed. On the other hand, for panels (a) and (c), the overall dynamics can be described as follows. As the initial wave profile starts propagating, a rarefaction fan is generated. After a specific time ("breaking time"  $t_b$ ), the wave undergoes a shock and becomes discontinuous. The subsequent interaction between the shock wave and the rarefaction wave ultimately yields a decrease in the overall amplitude of the initial profile. This mechanism is present either when compressible effects are negligible (lab scenario, Fig. 1(a)) and when compressible effects become relevant (atmospheric scenario, Fig. 1(c)). Compressibility brings forward the shock formation, so that its interaction with the rarefaction fan is triggered earlier in both space and time, thus providing a faster decrease in the amplitude of the wave. Additionally, the arrival time of the wave at a shoreline (x = 7 for the case presented in panel (d)) increases as function of  $\mu$ . In this regards, the inclusion of compressibility effects results in a more efficient way to attenuate, as well as slow down, the initial wave amplitude. A deeper insight into these features is provided in Section 3.2 and in Appendix B, where Burgers Eq. (20) is used to describe and compare these mechanisms, both qualitatively and quantitatively.

Another feature that emerges from the full numerical solutions is given by the importance of the initial width of the perturbation in the formation of the shock wave. Similarly to what happens for the compressibility parameter, the smaller the value of  $\sigma$ , the sooner the

shock will form producing a faster decrease of the wave amplitude in time.

More quantitatively, we show in Figs. 2 and 3 the error functions  $D_{\epsilon}$ and  $D_u$  for the three environments. For each scenario, nonlinear effects become non-negligible at times or order  $t \sim \mathcal{O}(1/\epsilon)$ , in accordance with the weakly nonlinear theory. It is interesting to notice though, that the larger  $\sigma$ , the more linear the behaviour of the waves within the spatio-temporal domain of the problem. In particular, the nonlinearity is almost absent for  $\sigma \geq 1$ . This does not necessarily mean that mathematically a shock would not occur at larger  $\sigma$ , but, for the specific environments considered, the breaking time would be out of a realistic time window. Regarding the effects of compressibility, the flow in the laboratory environment can be considered incompressible, as the error is at most of order  $\sim 10^{-6}$ . In the case of an ocean, the flow can be considered weakly compressible (error of order  $\sim 10^{-2}$ ). For the atmospheric case, the flow is fully compressible and the error is of order one all over the range of parameters investigated. Within this range the error seems to scale as  $\mu$ . To verify this trend we plot in Fig. 4 the  $L^2$ -norm of the error between the compressible and the incompressible solutions in the space–time domain  $\Omega_t = [-L, L] \times (0, t_f)$ , with  $t_f = 8$ . By fitting the numerical curve, we are also able to find the approximate analytical expression

$$\|\eta - \eta_i\|_{L^2(\Omega_t)}^{\text{(analytical)}} = -1.8066e^{-2.3258\mu} + 0.0252\mu + 1.8066.$$
 (42)

When  $0 \le \mu \ll 1$ , the error goes as a linear function of  $\mu$ , while for  $\mu \simeq \mathcal{O}(1)$  the exponential part becomes dominant and decreases the slope of the curve. Regarding the three specific environments considered, the

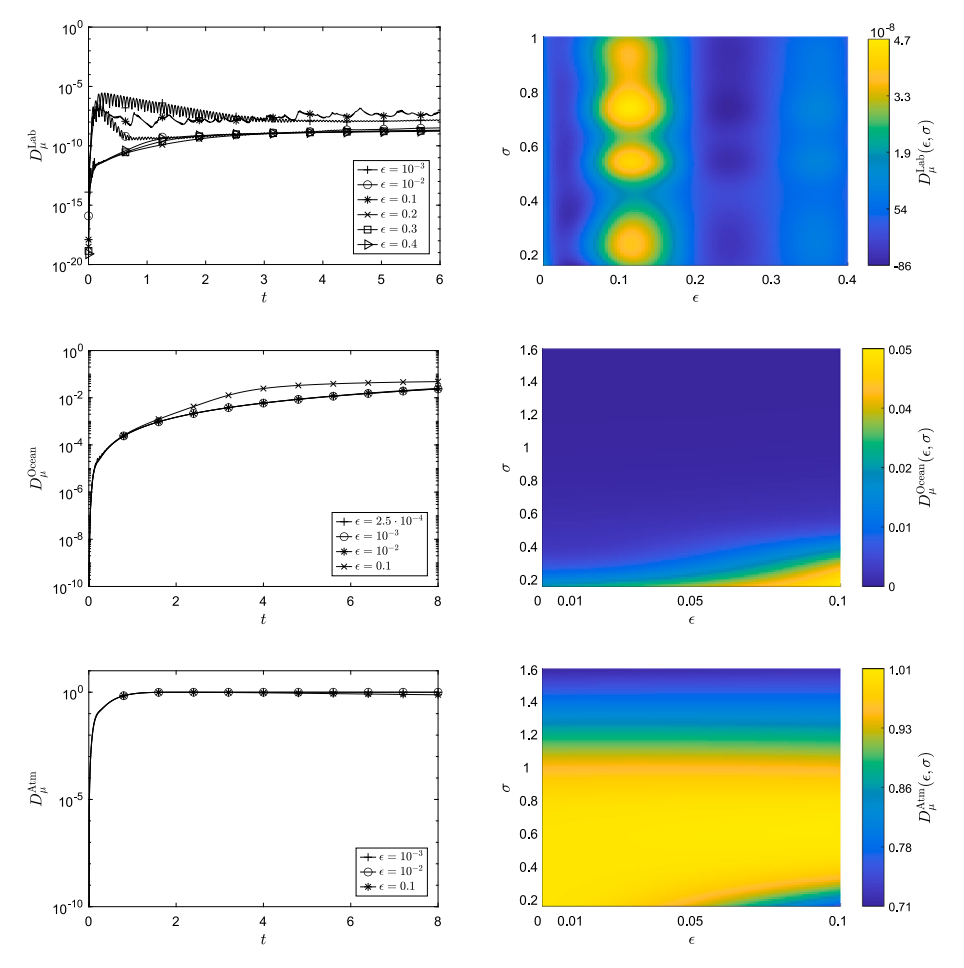


Fig. 3. Error function  $D_{\mu}^{\text{Lab}}$ ,  $D_{\mu}^{\text{Ocean}}$ ,  $D_{\mu}^{\text{Atm}}$  for the three scenarios. Left panels: logarithmic behaviour in time for  $\sigma = 1/2\pi$  and different  $\epsilon$ . Right panels: error behaviour at the final simulation time as function of  $\sigma$  and  $\epsilon$ .

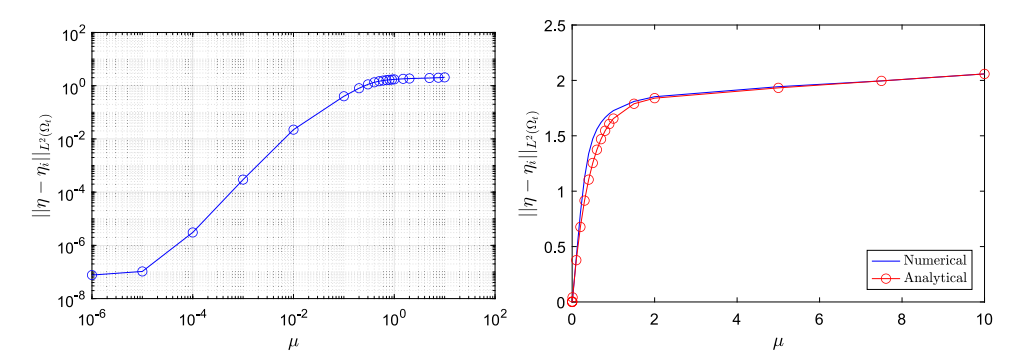


Fig. 4. Trend of the error  $\|\eta - \eta_i\|_{L^2(\Omega_i)}$  between compressible and incompressible solutions. Left: plot on a log-log scale. Right: plot on a linear scale and comparison with the analytical expression (42).

atmosphere poses the most stringent limitations in using incompressible equations. Thus, atmospheric surface waves should be modelled by taking into account compressible effects, resulting in a considerable variation of the wave properties. Nevertheless, even oceanic surface waves can be influenced by compressibility over long spatio-temporal scales, with improved estimation of arrival time and amplitude at shorelines.

#### 3.2. Results for model 1: comparison with Burgers equation

In this section we compare solutions coming from the full numerical simulations with those coming from the compressible Burgers Eq. (20)

with initial condition  $\eta_B(\xi,0)=0.5e^{-\xi^2/\sigma^2}$ . Even in this case, we define the  $L_2$ -error between the two families of solutions as

$$D_{\text{Burgers}}(t;\epsilon,\sigma,\mu) = \int_0^L |\eta(x,t;\sigma,\mu) - \eta_B(x,t;\epsilon,\sigma,\mu)|^2 dx / \int_0^L |\eta(x,\bar{t};\sigma,\mu)|^2 dx,$$
(43)

where  $\eta_B(x,t) \equiv A(x-c_\mu t, \varepsilon \tau)$  coincides with the solutions from Burgers equation and  $\bar{t}$  is the time at which the splitting of the initial surface profile into right-left travelling waves in the full numerical simulations vanishes, and we can focus on tracking only the right-going one. Figs. 6–8 show comparison between the free surface elevation for the three different environments at different times and for several values of both

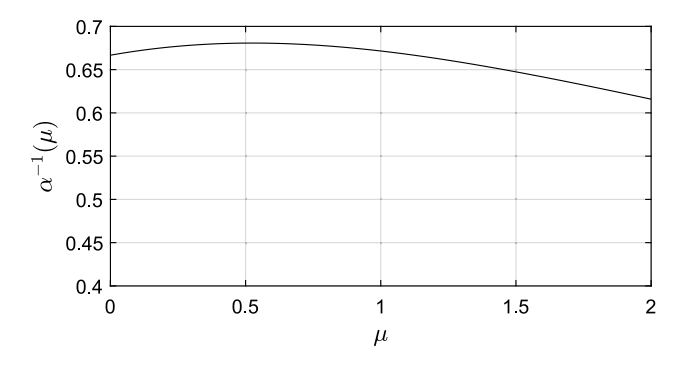


**Fig. 5.** Trend of the normalized breaking time  $\alpha^{-1}(\mu)$  according to Eq. (44).

 $\sigma$  and  $\varepsilon$ . Again, we push the values of  $\varepsilon$  beyond those achievable in real oceanic conditions so as to test the accuracy of the Burgers model. As can be noted, the agreement is excellent all over the entire range of parameters. The Burgers model is also capable of accurately capturing the shock formation given any initial gaussian profile, and to correctly follow the subsequent dynamics involving the interaction between a shock and a rarefaction wave (as explained in Section 3.1). Fig. 9 shows the  $L_2$ -error between the two solutions as function of time, computed for the most stringent case  $\sigma=1/2\pi$  and different values of  $\varepsilon$ . It can be noted that at most it reaches values of order  $\sim 10^{-2}$ , confirming the accuracy of Burgers solutions in describing the entire dynamics of these type of waves.

Using the Burgers equation, we can additionally compute the exact breaking time at which the shock occurs for the initial gaussian profiles [34]. This is given by

$$t_b(\epsilon, \sigma, \mu) = \frac{\sigma}{\epsilon \alpha(\mu)} \sqrt{2e}. \tag{44}$$

The trend of the normalized breaking time  $\alpha^{-1}(\mu)$  is shown in Fig. 5. As can be noted, there exists a local maximum for  $\mu \simeq 0.53$ , however for the three specific scenario considered in this work, this function is lower in the atmospheric case (highly compressible flow) with respect to the other two scenarios (weakly compressible flows).

Expression (44) contains most of the features already explained in Section 3.1 and recalled hereafter. 1) The higher the nonlinear coefficient  $\epsilon$ , the sooner the shock forms. 2) The higher the compressibility  $\mu$ , the sooner the shock forms. 3) The lower the width  $\sigma$  of the initial profile, the sooner the shock forms. These features all lead to beneficial effects in terms of amplitude reduction.

#### 3.3. Results for model 2

In this section, we provide results concerning the propagation of weakly nonlinear, weakly dispersive compressible waves, as described by Eq. (38). The compressible KdV equation is solved again using the method of lines (MOL). Our numerical scheme is first tested against two cases: the exact soliton solution  $A_{\rm ex}(\xi,\tau)={\rm sech}^2\left[\sqrt{3/4}(\xi-\tau/2)\right]$ , and the double soliton solution computed in Trefethen [35, p. 112] using a spectral collocation method. In Fig. 10 (left) we show time history of the relative error between the exact soliton  $A_{\rm ex}$  and our numerical solution. The agreement is remarkable, with a maximum relative error of  $3.6\cdot 10^{-4}$ . In Fig. 10 (right) a comparison between the spectral solution for the double soliton and that computed using the method of lines is given at different times. As emerges from both panels, our numerical method works well and we rely on it hereafter to perform a broader set of computations.

The CKdV equation is solved using the same initial conditions as those for the Burgers equation, namely  $\eta(\xi,0)=0.5e^{-\xi^2/\sigma^2}$ , with variations in  $\mu$ ,  $\epsilon$ , and  $\sigma$ . We compare the solutions obtained from

the CB and CKdV models across the three different scenarios, as illustrated in Fig. 11(a, b, c). In both laboratory and ocean scenarios, the initial wave energy disperses into smaller amplitude oscillations, leading to attenuation of the leading front as it propagates downstream. Conversely, in the atmospheric case, the amplitude of the perturbation slowly increases after initiation, ultimately resulting in the formation of two solitons, with the leading one exhibiting a significantly larger amplitude than the trailing one (Fig. 11(d)), in agreement with theoretical predictions [36]. Additionally, Fig. 11(d) confirms that high compressibility values decrease the wave speed even in a weakly dispersive regime.

These features can be formally justified by the presence of the term  $\beta(\mu)\partial_\xi^3$  on the right-hand side of Eq. (38). This additional term contributes to a nonlinear dispersion relation ( $\omega = c_\mu k + \beta(\mu)k^3$ ), and it also enables the existence of soliton solutions. The differing behaviours observed across the three environments stem from variations in the importance of compressibility. Specifically, for non-negligible values of the compressibility parameter  $\mu$ , solitons with increasing amplitudes may form.

To quantify this mechanism and relate it to the parameters  $\epsilon$  and  $\sigma$ , Fig. 12 presents the difference in maximum free surface deformation as a function of  $\sigma$ , computed within the simulation time window. The figure shows that for  $\epsilon=0.001,0.01,0.1$ , there exist values of  $\sigma$  for which this difference is positive, indicating amplification of the initial profile. This contrasts with the non-dispersive case, where larger values of  $\sigma$  delay shock formation and preserve the maximum wave amplitude at its initial value.

Finally, it is worth mentioning that if the nonlinearity is sufficiently strong or the initial profile is highly localized in space, the leading soliton may undergo a dispersive shock [37]. However, this does not occur within the range of parameters considered here for the three different environments.

#### 4. Conclusions

We have investigated the influence of fluid compressibility on the propagation of weakly nonlinear shallow-water waves, extending the classical shallow-water equations to incorporate compressibility effects. This extension enables a more accurate representation of wave dynamics in scenarios where compressibility cannot be neglected.

Our analysis yields two primary sets of equations: (1) A nondispersive model that generalizes the traditional incompressible shallow-water equations by accounting for compressibility. This model is particularly suitable for analysing long-wavelength waves where dispersive effects are minimal. (2) A weakly dispersive model that incorporates both compressibility and dispersion, providing a more comprehensive framework for studying wave phenomena where dispersion plays a significant role.

These formulations provide a robust foundation for exploring the intricate interplay between nonlinearity, compressibility, and dispersion in shallow-water wave propagation. For both systems, we have derived two reduced models to facilitate the analysis of their dynamics:

- The Burgers equation for non-dispersive waves, extending the classical shallow-water equations by incorporating compressibility effects.
- The Korteweg-de Vries (KdV) equation for weakly dispersive waves, capturing the balance between nonlinearity and dispersion in a compressible fluid context.

A convergence study between the Burgers model and the full set of compressible shallow-water equations was conducted to assess the accuracy of the reduced model. The results demonstrated high fidelity, even beyond the regime of weak nonlinearity (e.g., when the nonlinearity parameter  $\epsilon$  is of order one,  $\epsilon \sim \mathcal{O}(1)$ ). This suggests that the

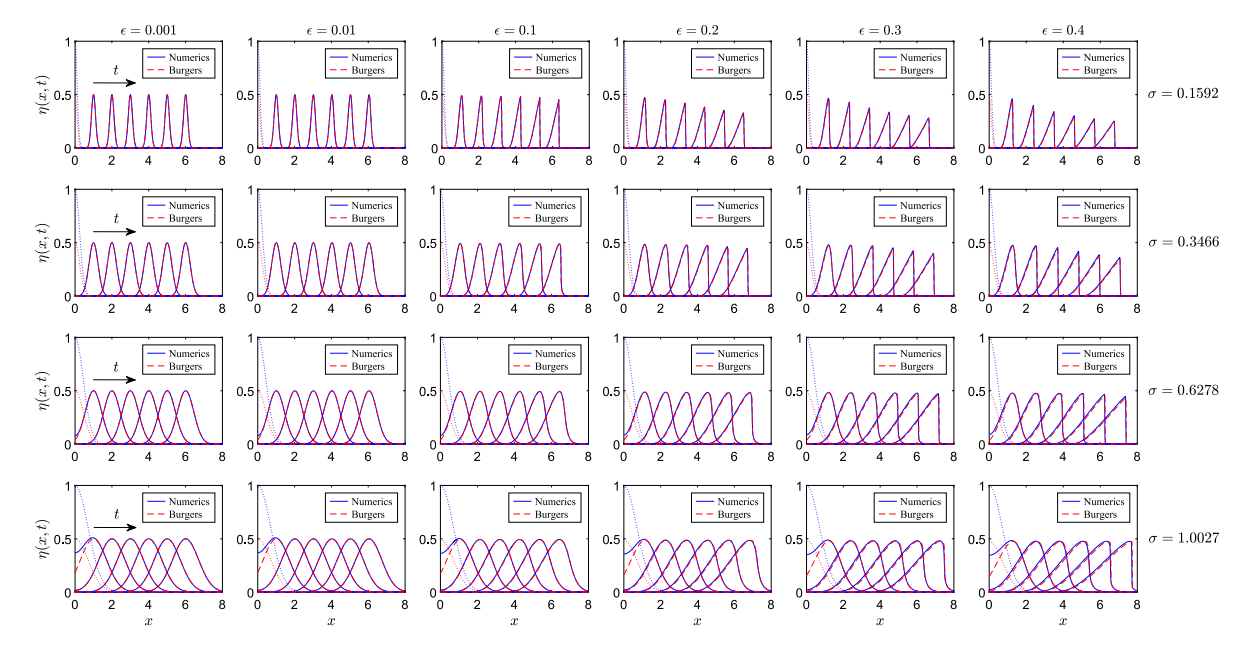


**Fig. 6.** Comparison between solutions coming from the full numerical simulations of Eqs. (13) and those coming from Burgers Eq. (20) for the lab scenario ( $\mu = 6.54 \cdot 10^{-6}$ ). The blue-dotted line represents the initial profile for the full numerical simulation. The red-dotted curve represents the initial profile for the Burgers simulation. The profiles are shown at different times, with a black arrow indicating the direction of increasing times. (For interpretation of the references to colour in this figure legend, the reader is referred to the web version of this article.)

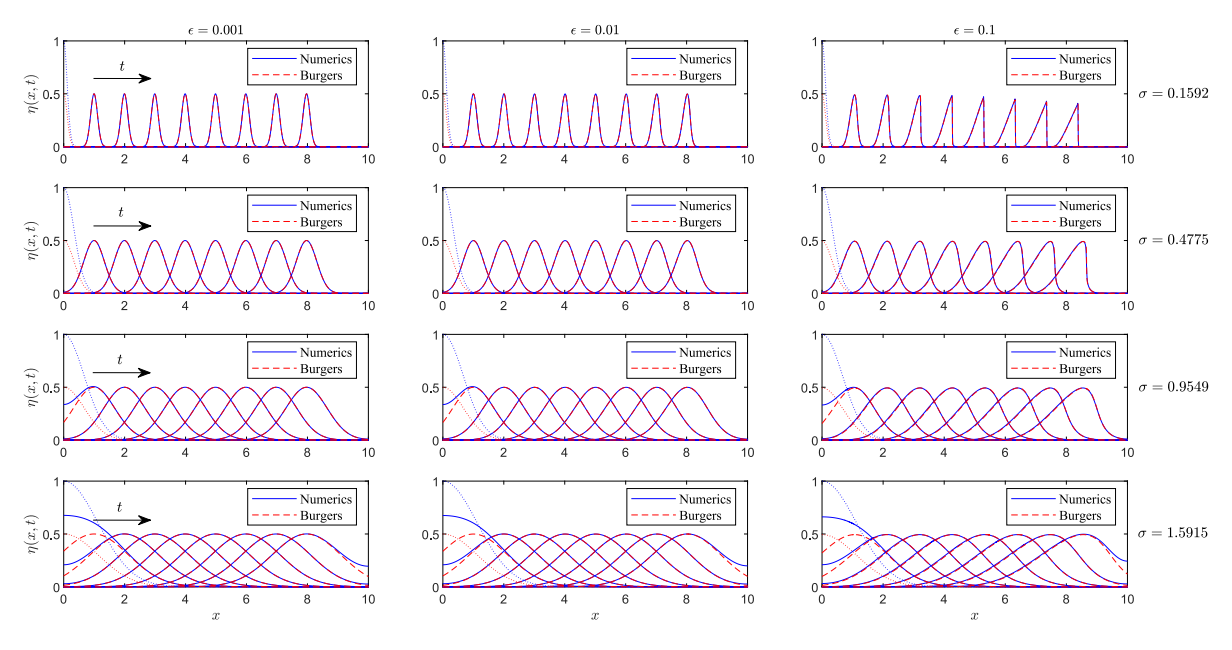


**Fig. 7.** Comparison between solutions coming from the full numerical simulations of Eqs. (13) and those coming from Burgers Eq. (20) for the ocean scenario ( $\mu = 0.01744$ ). The blue-dotted line represents the initial profile for the full numerical simulation. The red-dotted curve represents the initial profile for the Burgers simulation. The profiles are shown at different times, with a black arrow indicating the direction of increasing times. (For interpretation of the references to colour in this figure legend, the reader is referred to the web version of this article.)

reduced model remains effective in capturing the essential dynamics of the system under stronger nonlinear conditions.

The primary conclusion of this study is that fluid compressibility significantly influences the nonlinear propagation of shallow-water waves, distinguishing it from the traditional incompressible assumption. These differences manifest in both wave speed and amplitude. Our analysis demonstrates that compressibility impacts non-dispersive and weakly dispersive waves differently, necessitating distinct modelling approaches for each case.

In the non-dispersive regime, higher values of the compressibility parameter  $\mu$  accelerate the formation of shock waves and their interaction with rarefaction waves, ultimately leading to wave breaking and a reduction in amplitude. Overall, the wave is slowed down for higher values of  $\mu$  and the arrival time at a given spatial location is higher. Conversely, in the weakly dispersive regime, increased compressibility can amplify the initial perturbation, resulting in the formation of a discrete number of solitons. This phenomenon is particularly relevant in atmospheric waves, where compressibility plays a central role. In

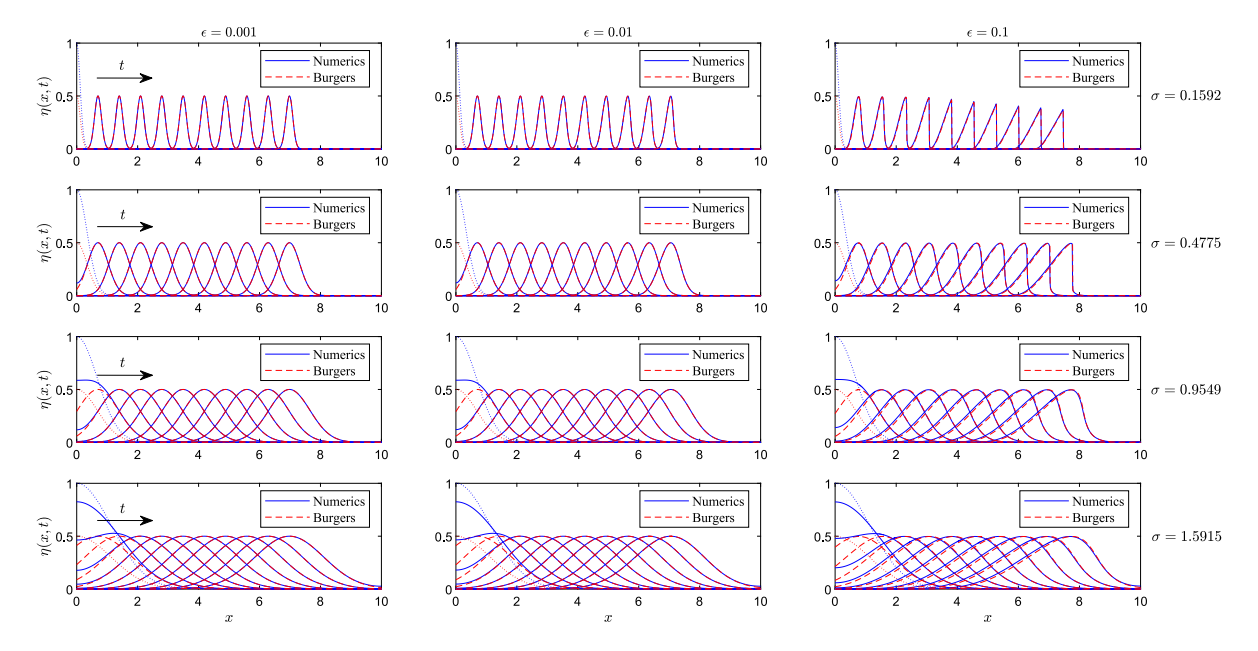


Fig. 8. Comparison between solutions coming from the full numerical simulations of Eqs. (13) and those coming from Burgers Eq. (20) for the atmosphere scenario ( $\mu = 1.6677$ ). The blue-dotted line represents the initial profile for the full numerical simulation. The red-dotted curve represents the initial profile for the Burgers simulation. The profiles are shown at different times, with a black arrow indicating the direction of increasing times. (For interpretation of the references to colour in this figure legend, the reader is referred to the web version of this article.)

contrast, for oceanic waves and surface waves generated in laboratory settings, the flow is nearly incompressible. In such cases, an initial perturbation tends to dissipate its energy into smaller trailing waves, leading to a gradual decrease in amplitude. Regarding wave speed and arrival time, the same trend as in the non-dispersive regime is observed when dispersion is weak but non-negligible, with waves being slower for higher values of  $\mu$  (Fig. 11(d)).

Other parameters, such as the dimensionless wave amplitude  $\epsilon$  and the width of the initial perturbation  $\sigma$ , may influence the aforementioned dynamics. To quantify these effects on both types of waves, a parametric study has been conducted. In the non-dispersive case, higher values of  $\epsilon$  and lower values of  $\sigma$  accelerate shock formation, leading to beneficial results in terms of amplitude reduction. In the dispersive case, greater values of both  $\epsilon$  and  $\sigma$  result in multiple solitons, each exhibiting a peak significantly larger than the maximum amplitude of the initial perturbation.

There remain opportunities to improve the models derived in this work to achieve a more accurate description of shallow-water flow dynamics and their applications in modelling real phenomena, such as tsunamis. One possibility is to include the elasticity of the seabed, obtaining a reduced system of equations that describe both the free surface elevation of the fluid and that of the seabed. Another possibility is to include Earth rotation. Additionally, conducting laboratory experiments for the cases presented in this work would further contribute to validating the developed theory.

Furthermore, investigating potential resonance mechanisms between elastic and compressible-gravity modes would be both interesting and beneficial from an applied perspective, with the aim of enhancing the design and reliability of tsunami early warning systems.

Finally, a more theoretical avenue involves extending the validity of the models presented herein to scenarios where dispersive and/or nonlinear effects are no longer weak.

#### CRediT authorship contribution statement

**E. Zuccoli:** Writing – original draft, Methodology, Formal analysis, Conceptualization. **U. Kadri:** Writing – original draft, Supervision, Methodology, Formal analysis, Conceptualization.

#### **Funding:**

This work was supported by the Leverhulme Trust Research Project Grant number 523930.

#### **Declaration of competing interest**

The authors declare that they have no known competing financial interests or personal relationships that could have appeared to influence the work reported in this paper.

## Appendix A. Numerical methods for the compressible shallow water equations

#### A.1. Roe's numerical scheme

Consider the system of Eqs. (13) in one spatial dimension. Following [2], it can be written in conservative form as

$$\partial_t H + \partial_x (vH) = 0,$$
 (A.1a)

$$\partial_t(vH) + \partial_x \left[ v^2 H + \frac{1}{u} \left( H - \frac{g}{u} \log(1 + \mu H) \right) \right],$$
 (A.1b)

where  $H = (e^{\mu(\epsilon\eta+1)} - 1)/\mu$ ,  $v = \epsilon u$  and  $g \in \mathbb{R}$  is a coefficient written here only for test purposes (g = 1) in the actual non-dimensional compressible shallow-water Eqs. (13)). We define the momentum per unit volume m = vH and introduce the state vector  $\boldsymbol{w} = (H, m)^T$ , so that Eqs. (A.1) can be compactly written as

$$\partial_t \boldsymbol{w} + \partial_x \boldsymbol{f}(\boldsymbol{w}) = 0, \tag{A.2}$$

where the flux function takes the form

$$f(\boldsymbol{w}) = \left(m, \frac{m^2}{H} + \frac{1}{\mu} \left(H - \frac{g}{\mu} \log(1 + \mu H)\right)\right)^T. \tag{A.3}$$

To solve (A.2) we apply a finite-difference scheme with Roe's numerical flux [28,38].

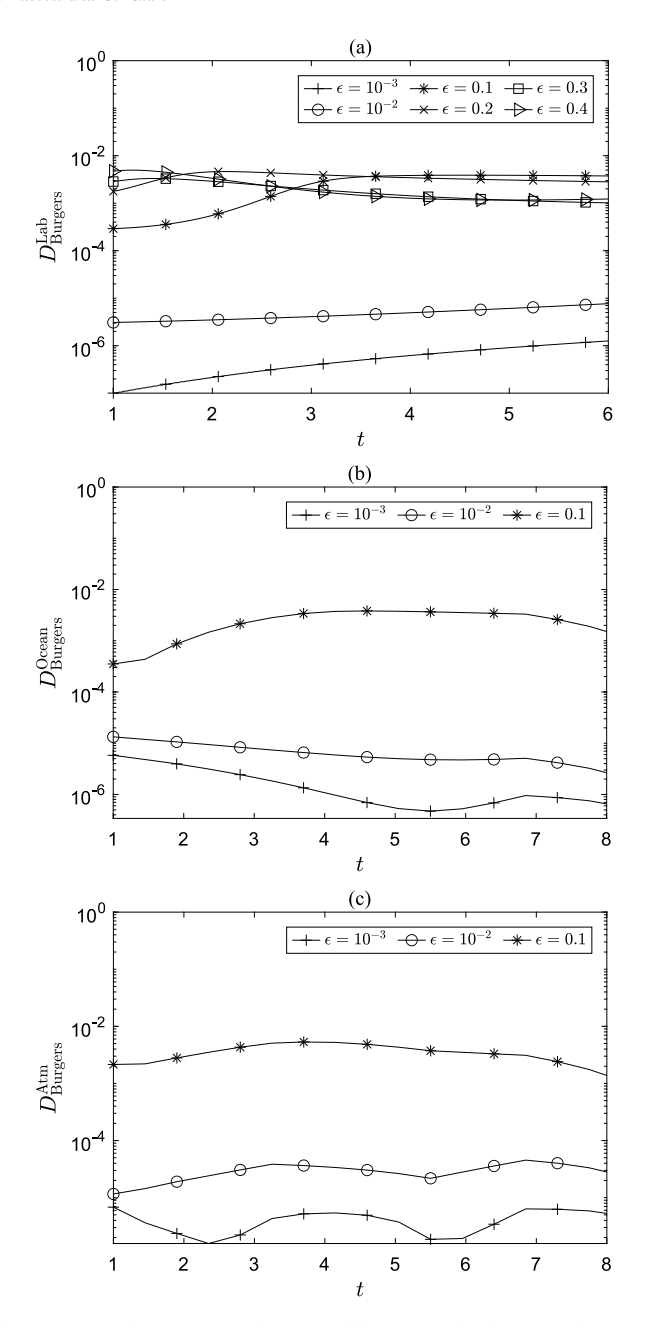


**Fig. 9.** Logarithmic  $L_2$ -error between full numerical solutions and Burgers solutions computed at  $\sigma=1/2\pi$  and different  $\epsilon$ . (a): lab environment. (b): ocean environment. (c): atmospheric environment.

#### A.2. Method of lines

Another approach to solve system (13) is to introduce an artificial viscous term of the form  $v\partial_x^2 u$  on the right-hand side of (13a) and implementing the method of lines with a centred finite difference discretization in space [39]. The artificial viscosity v is tuned in order to properly capture the shocks formation and, at the same time, to avoid dispersion and extreme dissipation. In particular, for the results shown in Section 3.1,  $v = \gamma dx$ , with  $\gamma = 5$  when  $\sigma = 1/2\pi$  and  $\gamma = 1$  in all other cases.

The two numerical schemes have then been tested against "problem A" contained in Hudson [40, pp. 4–6], giving both accurate and reliable results, as shown in Fig. A.13. For such a test case, parameters are  $\mu=0$ ,

 $\epsilon = 1$  and g = 9.81, whereas the initial conditions are

$$m(x,0) = 0$$
, and  $H(x,0) = \begin{cases} 1, & x \le 1/2, \\ \frac{1}{2}, & x > 1/2. \end{cases}$  (A.4)

Each scheme is capable of capturing both shock and rarefaction waves without introducing too much dissipation. The MOL, however, was computationally faster and less dissipative for larger times (even for computing linear solutions of (13)), hence we preferred to employ that in the large parametric study conducted in Section 3.

#### Appendix B. Exact Burgers solution for a triangular wave

In this section we want to provide more insight and justification for the features shown in the results Section 3.1 about the propagation of weakly nonlinear, non-dispersive, compressible waves. To carry out such objective, we study here the Burgers Eq. (20) subject to a triangular wave initial condition, such that its solution can be obtained analytically in closed form. Using the method of characteristics [34], the exact solution can be split in two parts: the solution valid before the formation of a shock, and the solution valid after that. The point in space–time where the shock forms is given by  $(\xi_b, \tau_b) = (\sigma \sqrt{\pi}, 2\sigma \sqrt{\pi}/\alpha(\mu))$ , where  $\sigma$  is the non-dimensional wavelength of the initial wave profile. So, the solution before the shock formation  $(\tau < \tau_b)$  reads:

$$A(\xi,\tau) = \begin{cases} 0, & \xi < -\sigma\sqrt{\pi}, \\ \frac{1}{2\sigma\sqrt{\pi}} \left[ \frac{\xi + \sigma\sqrt{\pi}}{1 + \frac{\alpha(\mu)}{2\sigma\sqrt{\pi}} \tau} \right], & -\sigma\sqrt{\pi} \le \xi \le \alpha(\mu)\tau/2, \\ \frac{1}{2\sigma\sqrt{\pi}} \left[ \frac{\sigma\sqrt{\pi} - \xi}{1 - \frac{\alpha(\mu)}{2\sigma\sqrt{\pi}} \tau} \right], & \alpha(\mu)\tau/2 \le \xi \le \sigma\sqrt{\pi}, \\ 0, & \xi \ge \sigma\sqrt{\pi}. \end{cases}$$
(B.1)

The solution after the shock formation  $(\tau \ge \tau_b)$  reads:

$$A(\xi,\tau) = \begin{cases} 0, & \xi < -\sigma\sqrt{\pi}, \\ \frac{1}{2\sigma\sqrt{\pi}} \left[ \frac{\xi + \sigma\sqrt{\pi}}{1 + \frac{\alpha(\mu)}{2\sigma\sqrt{\pi}} \tau} \right], & -\sigma\sqrt{\pi} \le \xi \le \xi_s(\tau), \\ 0, & \xi \ge \xi_s(\tau), \end{cases}$$
(B.2)

where  $\xi_s(\tau)$  is the shock path and is given by

$$\xi_s(\tau) = -\sigma\sqrt{\pi} + 2^{1 - 1/2\alpha(\mu)}\sigma\sqrt{\pi} \left(1 + \frac{\alpha(\mu)\tau}{2\sigma\sqrt{\pi}}\right)^{1/2\alpha(\mu)}, \quad \tau \ge \frac{2\sigma\sqrt{\pi}}{\alpha(\mu)}. \quad (B.3)$$

The complete space-time diagram is displayed in Fig. B.14(left), together with the solution at different times (right).

From this analysis, two features can be noted: as the wave is initialized, a rarefaction fan starts propagating, with the characteristics changing slopes smoothly. Simultaneously, the wave does not change amplitude, but simply approaches a discontinuity point. When the discontinuity is met, a shock wave occurs and starts interacting with the rarefaction wave, producing an overall decreasing of the wave amplitude in time. This simple exercise provides additional evidence of the overall dynamics of more realistic waves discussed in Section 3.

#### Appendix C. Burgers energy equation at shock

Let us consider the compressible Burgers equation in quasilinear form (20). Under the change of variables  $T=\alpha(\mu)\tau$  and  $A(\xi,\tau(T))=\varphi(\xi,T)$ , it reduces to the standard Burgers equation

$$\partial_T \varphi + \varphi \partial_{\varepsilon} \varphi = 0, \tag{C.1}$$

which can be re-written (after multiplying it by  $\varphi$ ) as

$$\partial_T \left( \frac{\varphi^2}{2} \right) + \partial_{\xi} \left( \frac{\varphi^3}{3} \right) = 0. \tag{C.2}$$

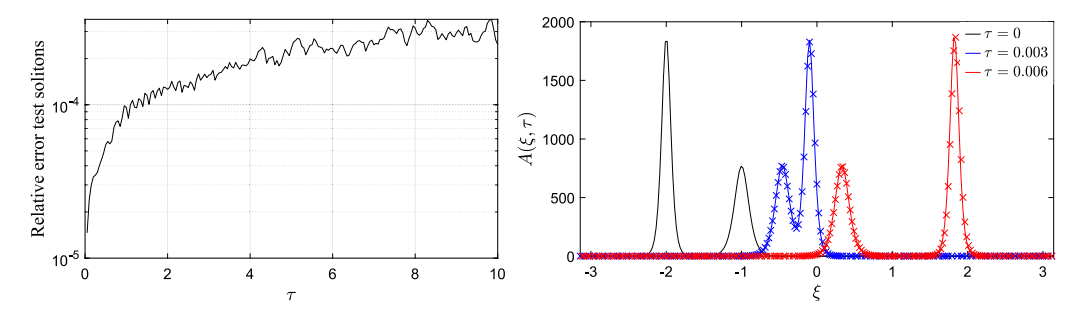
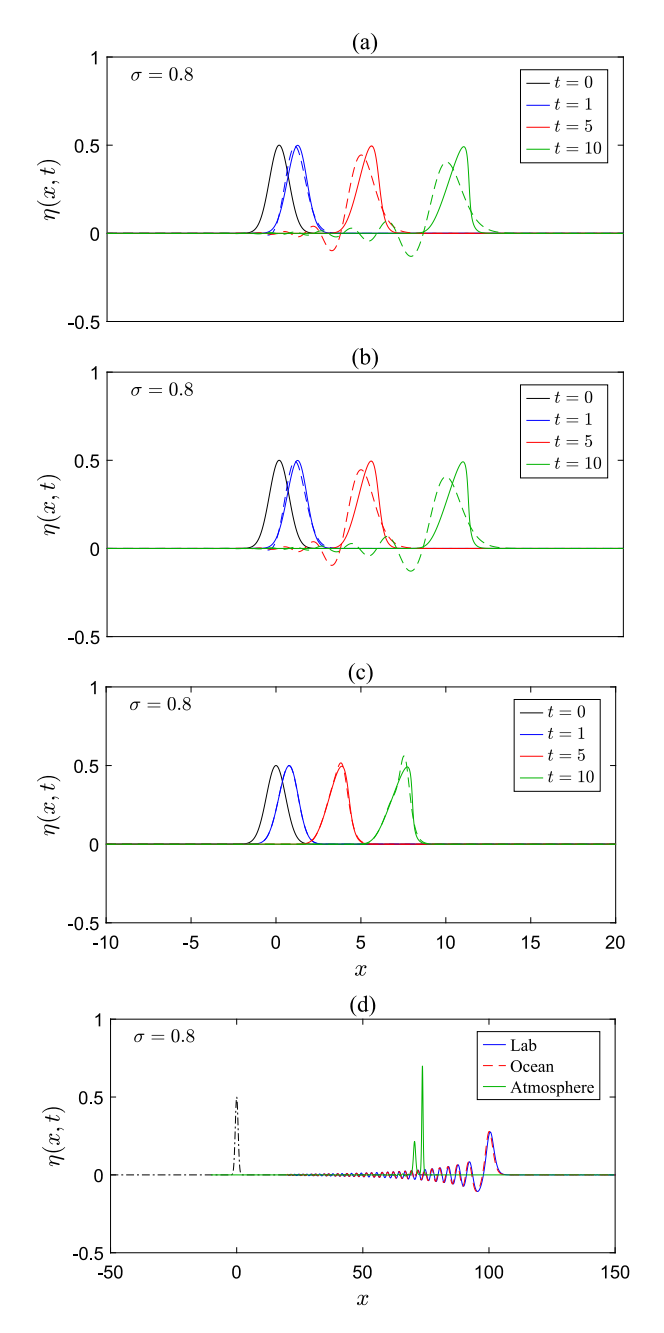


Fig. 10. Left: relative error between the exact soliton solution  $A_{ex}$  and the corresponding numerical solution as function of time. Right: comparison of the double soliton solution in Trefethen [35, p. 112] computed using the MOL (full lines) and a collocation spectral method (x markers).



**Fig. 11.** (a)–(b)–(c): comparison between Burgers and KdV solutions in lab, ocean and atmospheric conditions, respectively, for  $\epsilon=0.1$ . Full lines: compressible Burgers; dashed lines: compressible KdV. (d): comparison of CKdV solutions at a larger time t=100 for the three scenarios. Dash-dotted line represents the initial condition.

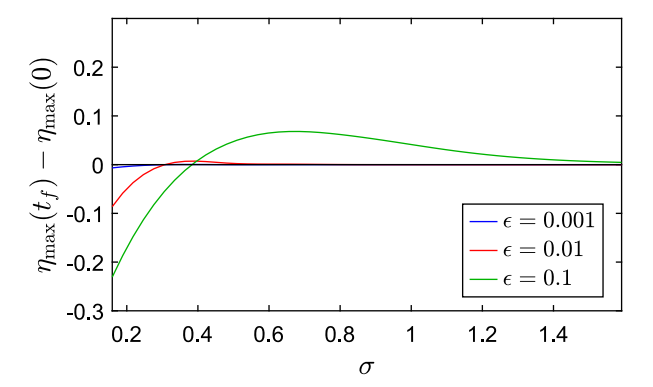
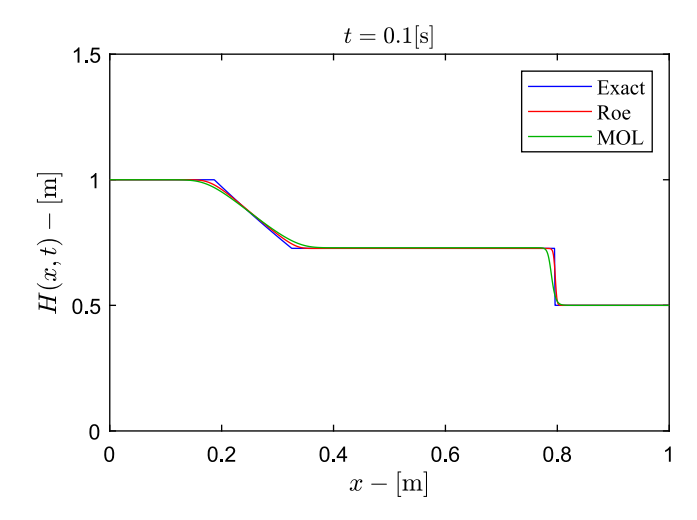


Fig. 12. Difference between the final maximum amplitude  $(t_f=10)$  and the initial maximum amplitude for atmospheric waves as function of the initial perturbation width  $\sigma$ , for three values of  $\epsilon$ .



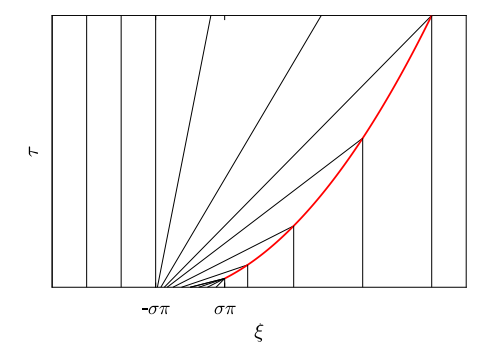
**Fig. A.13.** Comparison between exact and numerical solutions for "problem A" in Hudson [40]. Initial condition is given by (A.4), with parameters  $\epsilon=1$ ,  $\mu=0$  and g=9.81. Solutions are plotted at time t=0.1.

Assuming a shock wave occurs, we integrate Eq. (C.2) along  $\xi \in (-\infty, +\infty)$  on both sides of the shock, obtaining

$$\frac{\mathrm{d}}{\mathrm{d}T} \int_{-\infty}^{+\infty} \frac{\varphi^2}{2} \mathrm{d}\xi + \frac{\dot{S}}{2} (\varphi_+^2 - \varphi_-^2) + \frac{1}{3} (\varphi_-^3 - \varphi_+^3) = 0, \tag{C.3}$$

where  $\dot{S}$  is the shock speed and  $\varphi_{\pm}$  are the finite values of  $\varphi$  just after and before the shock, respectively. We define the energy  $E=\frac{\mathrm{d}}{\mathrm{d}T}\int_{-\infty}^{+\infty}\frac{\varphi^2}{2}\mathrm{d}\xi$ , and, recalling that  $\dot{S}=\frac{\varphi_{+}+\varphi_{-}}{2}$  [34], Eq. (C.3) becomes

$$\frac{\mathrm{d}E}{\mathrm{d}T} = -(\varphi_{-} - \varphi_{+}) \left[ -\frac{1}{4} (\varphi_{-} + \varphi_{+})^{2} + \frac{1}{3} (\varphi_{-}^{2} + \varphi_{-} \varphi_{+} + \varphi_{+}^{2}) \right]. \tag{C.4}$$



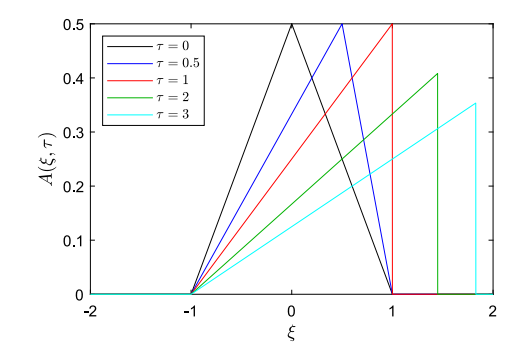


**Fig. B.14.** Triangular wave problem for Burgers equation. (Left): characteristics diagram, with the shock path  $\xi_s(\tau)$  shown in red. (Right): solution at different times. Full lines: exact analytical solution. Dots: numerical solution using Roe's scheme. (For interpretation of the references to colour in this figure legend, the reader is referred to the web version of this article.)

After re-arranging the expression in square brackets, we obtain the final energy equation

$$\frac{dE}{dT} = -\frac{1}{12}(\varphi_{-} - \varphi_{+})^{3} < 0, \tag{C.5}$$

since  $\varphi_- > \varphi_+$  for shocks to occur [41]. Eq. (C.5) shows that energy always decreases when a shock occurs.

#### Data availability

No data was used for the research described in the article.

#### References

- [1] A.J.C. Barré de Saint-Venant, Theorie du mouvement non permanent des eaux, avec application aux crues des rivieres et a l'introduction de marees dans leurs lits, C. R. Acad. Sci. Paris 73 (1871) 147–151.
- [2] R. LeVeque, Numerical methods for conservation laws, seconnd ed., in: Lectures in Mathematics. ETH Zürich, Birkhäuser Basel, 1992, 1992.
- [3] V.V. Titov, C.E. Synolakis, Numerical modeling of tidal wave runup, J. Waterw. Port Coast. Ocean. Eng. 124 (4) (1998) 157–171, http://dx.doi.org/10.1061/ (ASCE)0733-950X(1998)124:4(157).
- [4] S. Turitsyn, A. Bednyakova, E. Podivilov, Nonlinear optical pulses in media with asymmetric gain, Phys. Rev. Lett. 131 (15) (2023) http://dx.doi.org/10.1103/ PhysRevLett.131.153802.
- [5] J. Boussinesq, Theorie de l'intumescence liquide, applelee onde solitaire ou de translation, se propageant dans un canal rectangulaire, C. R. Acad. Sci. Paris 72 (1871) 755-750
- [6] C.H. Su, C.S. Gardner, Korteweg-de Vries equation and generalizations. III. Derivation of the Korteweg-de Vries equation and Burgers equation, J. Math. Phys. 10 (3) (1969) 536–539, http://dx.doi.org/10.1063/1.1664873.
- [7] A.E. Green, P.M. Naghdi, A derivation of equations for wave propagation in water of variable depth, J. Fluid Mech. 78 (2) (1976) 237–246, http://dx.doi. org/10.1017/S0022112076002425.
- [8] P. Bonneton, F. Chazel, D. Lannes, F. Marche, M. Tissier, A splitting approach for the fully nonlinear and weakly dispersive Green-Naghdi model, J. Comput. Phys. 230 (4) (2011) 1479–1498, http://dx.doi.org/10.1016/j.jcp.2010.11.015.
- [9] M. Brocchini, A reasoned overview on Boussinesq-type models: The interplay between physics, mathematics and numerics, Proc. R. Soc. A: Math. Phys. Eng. Sci. 469 (2160) (2013) http://dx.doi.org/10.1098/rspa.2013.0496.
- [10] J.T. Kirby, Boussinesq models and their application to coastal processes across a wide range of scales, J. Waterw. Port Coast. Ocean. Eng. 142 (6) (2016) http://dx.doi.org/10.1061/(ASCE)WW.1943-5460.0000350.
- [11] J.C. McWilliams, Fundamentals of Geophysical Fluid Dynamics, Cambridge University Press, 2006.
- [12] C. Raupp, P. Silva Dias, E. Tabak, P. Milewski, Resonant wave interactions in the equatorial waveguide, J. Atmos. Sci. 65 (11) (2008) 3398–3418, http: //dx.doi.org/10.1175/2008JAS2387.1.
- [13] C. Raupp, P. Silva Dias, Resonant wave interactions in the presence of a diurnally varying heat source, J. Atmos. Sci. 66 (10) (2009) 3165–3183, http://dx.doi.org/ 10.1175/2009JAS2899.1.
- [14] R.S. Johnson, Shallow water waves on a viscous fluid The undular bore, Phys. Fluids 15 (10) (1972) 1693–1699, http://dx.doi.org/10.1063/1.1693764.
- [15] D. Dutykh, Mathematical Modelling of Tsunami Waves (Ph.D. thesis), École normale supérieure de Cachan - ENS Cachan, 2007, URL: https://theses.hal. science/tel-00194763.

- [16] U. Kadri, M. Stiassnie, Generation of an acoustic-gravity wave by two gravity waves, and their subsequent mutual interaction, J. Fluid Mech. 735 (2013) R6, http://dx.doi.org/10.1017/jfm.2013.539.
- [17] U. Kadri, T. Akylas, On resonant triad interactions of acoustic-gravity waves, J. Fluid Mech. 788 (2016) http://dx.doi.org/10.1017/jfm.2015.721.
- [18] U. Kadri, Triad resonance between a surface-gravity wave and two high frequency hydro-acoustic waves, Eur. J. Mech. B Fluids 55 (2016) 157–161, http://dx.doi.org/10.1016/j.euromechflu.2015.09.008.
- [19] U. Kadri, Tsunami mitigation by resonant triad interaction with acoustic-gravity waves, Heliyon 3 (2017) http://dx.doi.org/10.1016/j.heliyon.2017.e00234.
- [20] D. Andrade, M. Bustamante, U. Kadri, R. Stuhlmeier, Acoustic-gravity wave triad resonance in compressible flow: A dynamical systems approach, J. Fluid Mech. 1013 (2025) http://dx.doi.org/10.1017/jfm.2025.10259.
- [21] E. Zuccoli, U. Kadri, Resonant triad interactions of two acoustic modes and a gravity wave, J. Fluid Mechancis 1008 (2025) A15, http://dx.doi.org/10.1017/ jfm.2025.111.
- [22] M.S. Longuet-Higgins, A theory of the origin of microseisms, Philos. Trans. R. Soc. Lond. Ser. A Math. Phys. Sci. 243 (857) (1950) 1–35.
- [23] R. Johnson, A Modern Introduction to the Mathematical Theory of Water Waves, Cambridge University Press, 1997.
- [24] E. Hinch, Perturbation Methods, Cambridge University Press, 1991.
- [25] A.H. Nayfeh, Perturbation Methods, John Wiley & Sons, 2008.
- 26] F. Charru, Hydrodynamic Instabilities, vol. 37, Cambridge University Press, 2011.
- [27] G. Richard, An extension of the Boussinesq-type models to weakly compressible flows, Eur. J. Mech. B Fluids 89 (2021) 217–240, http://dx.doi.org/10.1016/j. euromechflu.2021.05.011.
- [28] D. Ambrosi, Approximation of shallow water equations by Roe's Riemann solver, Internat. J. Numer. Methods Fluids 20 (2) (1995) 157–168, http://dx.doi.org/ 10.1002/fld.1650200205.
- [29] D. Durran, Numerical Methods for Wave Equations in Geophysical Fluid Dynamics, vol. 32, Springer Science & Business Media, 1998.
- [30] A. Jameson, Energy estimates for nonlinear conservation laws with applications to solutions of the burgers equation and one-dimensional viscous flow in a shock tube by central difference schemes, in: Collection of Technical Papers - 18th AIAA Computational Fluid Dynamics Conference, vol. 2, 2007, pp. 2133–2157.
- [31] L. Quartapelle, L. Castelletti, A. Guardone, G. Quaranta, Solution of the Riemann problem of classical gasdynamics, J. Comput. Phys. 190 (1) (2003) 118–140, http://dx.doi.org/10.1016/S0021-9991(03)00267-5.
- [32] M. Fossati, L. Quartapelle, The Riemann problem for hyperbolic equations under a nonconvex flux with two inflection points, 2014, arXiv preprint arXiv:1402.
- [33] W.E. Schiesser, G.W. Griffiths, A Compendium of Partial Differential Equation Models: Method of Lines Analysis with Matlab, Cambridge University Press, 2009.
- [34] J. Logan, Applied Mathematics: a contemporary approach, John Wiley & Sons,
- [35] L. Trefethen, Spectral Methods in Matlab, Society for Industrial and Applied Mathematics, Philadelphia, PA, 2000.
- [36] A. Kundu, Tsunami and Nonlinear Waves, Springer, 2007.
- [37] M. Ablowitz, D. Baldwin, M. Hoefer, Soliton generation and multiple phases in dispersive shock and rarefaction wave interaction, Phys. Rev. E - Stat. Nonlinear Soft Matter Phys. 80 (1) (2009) http://dx.doi.org/10.1103/PhysRevE.80.016603.
- [38] A. Guardone, L. Vigevano, Roe linearization for the van der Waals gas, J. Comput. Phys. 175 (1) (2002) 50–78, http://dx.doi.org/10.1006/jcph.2001.6915.
- [39] E. Zuccoli, Free Surface Waves on Swirling Flows (Ph.D. thesis), University of Warwick, 2023, URL: https://wrap.warwick.ac.uk/185196, WRAP 185196.
- [40] J. Hudson, Numerical techniques for the shallow water equations, (2) 1999, pp. 1–65, https://www.reading.ac.uk/maths-and-stats/publications/numerical-analysis-reports#1999.
- [41] P.D. Lax, Hyperbolic systems of conservation laws II, Comm. Pure Appl. Math. 10 (4) (1957) 537–566, http://dx.doi.org/10.1002/cpa.3160100406.